ACS OMEGA

http://pubs.acs.org/journal/acsodf

Article

Defective Graphene/Plasmonic Nanoparticle Hybrids for Surface-Enhanced Raman Scattering Sensors

Ravi K. Biroju,* Bhanu Chandra Marepally, Pariksha Malik, Soumen Dhara, Saravanan Gengan, Dipak Maity, Tharangattu N. Narayanan, and Pravat K. Giri*

Cite This: *ACS Omega* 2023, 8, 4344−4356

Read Online

ACCESS | Metrics & More | Article Recommendations | Supporting Information

ABSTRACT: Two-dimensional−zero-dimensional plasmonic hybrids involving defective graphene and transition metals (DGR-TM) have drawn significant interest due to their near-field plasmonic effects in the wide range of the UV−vis−NIR spectrum. In the present work, we carried out extensive investigations on resonance Raman spectroscopy (RRS) and localized surface plasmon resonance (LSPR) from the various DGR-TM hybrids (Au, Ag, and Cu) using micro-Raman, spatial Raman mapping analysis, high-resolution transmission electron microscopy (HRTEM), and LSPR absorption measurements on defective CVD graphene layers. Further, electric field (E) mappings of samples were calculated using the finite domain time difference (FDTD) method to support the experimental findings. The spatial distribution of various in-plane and edge defects and defect-mediated interaction of plasmonic nanoparticles (NPs) with graphene were investigated on the basis of the RRS and LSPR and correlated with the quantitative analysis from HRTEM, excitation wavelength-dependent micro-Raman, and E-field enhancement features of defective graphene and defective graphene-Au hybrids before and after rapid thermal annealing (RTA). Excitation wavelength-dependent surface-enhanced Raman scattering (SERS) and LSPR-induced broadband absorption from DGR-Au plasmonic hybrids reveal the electron and phonon interaction on the graphene surface, which leads to the charge transfer from TM NPs to graphene. This is believed to be responsible for the reduction in the SERS signal, which was observed from the wavelength-dependent Raman spectroscopy/mappings. We implemented defective graphene and DGR-Au plasmonic hybrids as efficient SERS sensors to detect the Fluorescein and Rhodamine 6G molecules with a detection limit down to 10^{-9} M. Defective graphene and Au plasmonic hybrids showed an impressive Raman enhancement in the order of 10^{8}, which is significant for its practical application.

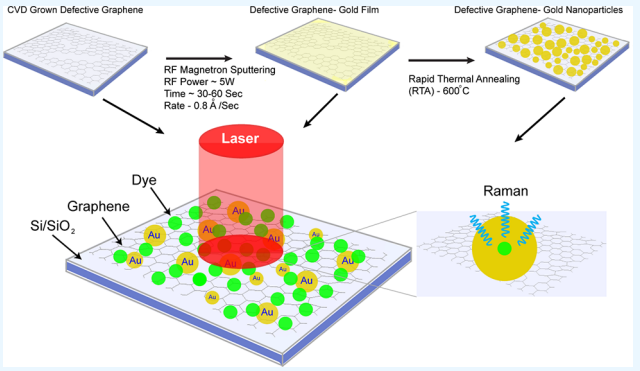

1. INTRODUCTION

The construction of transition metal (TM) plasmonic nanostructures (PNSs) incorporated with graphene is attracting considerable research attention for enhanced photocatalysis and photovoltaic applications.[1−3] However, ultrathin films and nanoparticles (NPs) of TM interfaced with graphene have been exploited for interesting properties in the graphene research community.[4,5] Various chemical and physical approaches have been developed to design graphene-plasmonic hybrids for enhanced optical and optoelectronic characteristics. Most of the experiments on fabrication were carried out by chemical approaches, and the contribution of graphene and its structural evolution is lacking in the recent reports on the graphene-TM PNSs.[5,6] Understanding the interaction of various TM films and NPs over the graphene layer preserving its high structural quality and the role of intrinsic defects using resonance Raman scattering (RRS) and localized surface plasmon resonance (LSPR) absorption techniques is challenging. On the other hand, the uniqueness of graphene having a high charge carrier mobility and a wide range of optical transparency over the visible to near-infrared (NIR) region makes it suitable for the resonance of surface plasmon originating from the TM PNSs in the visible excitation energy. These graphene-TM hybrid functional materials can show enhanced visible light photocatalytic activity and efficient photovoltaic effects incorporating various photosensitive nanomaterials.[7] As a result of the very high charge carrier mobility from the surface electrons on the graphene layer and the LSPR absorption from the various TM PNSs, ultrafast charge transfer from the resultant graphene-TM PNSs is facilitated when they get excited by the visible-NIR light source

Received: December 2, 2022
Accepted: January 4, 2023
Published: January 19, 2023

https://doi.org/10.1021/acsomega.2c07706
ACS Omega 2023, 8, 4344−4356

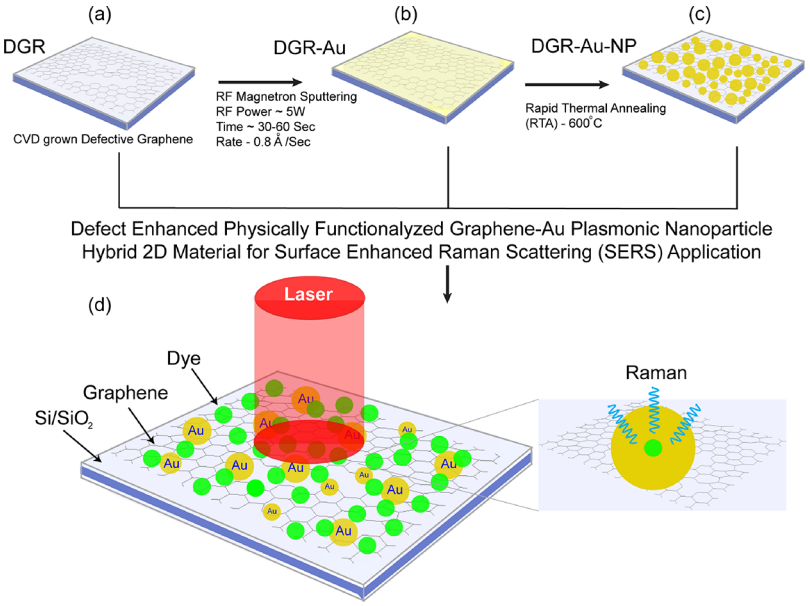

Figure 1. Schematic shows the fabrication of defective graphene-Au nanoparticle plasmonic hybrid for SERS application: (a) defective graphene (DGR) on the SiO_2 substrate, (b) deposition of a thin Au film on DGR, (c) RTA treatment of DGR-Au, and (d) SERS from the DGR-Au substrates.

depending upon the nature of TM and the size and shape of the NS. The structural defects on the graphene layer can give fascinating properties from this kind of graphene-TM PNSs.[7−13] For example, Gong *et. al* reported the hybrid structure of AgNPs and a few-layer graphene (FLG) to improve the performance of SERS substrates by making different ways of sandwiching the AgNPs with the FLG.[11,12] There are very few reports on the excitation wavelength-dependent RRS and LSPR absorption from the various graphene-TM PNSs and the role of intrinsic defects in graphene on the evolution of RRS and LSPR from the statistical evaluation of the defect density based on the Raman line shape and high-resolution Raman imaging of the various graphene-TM PNSs. The concept of physical functionalization of the CVD graphene with Au NPs mediated by the intrinsic defects on the graphene layer using physical and chemical approaches was recently demonstrated by the authors and other research groups.[7−9] We established the localization of Au NPs at the defect sites of the graphene layer using RRS of the D and D′ Raman bands. Interestingly, these kinds of functional hybrids are highly efficient for visible light photocatalysis.[4] In addition, we have established maximization of defect-enhanced Raman scattering of electrochemically deposited Au NPs on plasma [argon (Ar)/hydrogen (H_2) gas] treated CVD graphene. A SERS enhancement of up to $\sim 10^8$ to detect the solution-soaked R6G molecules was found.[9]

In the present study, we investigated the plasmonic effects of the surface-modified graphene with TM ultrathin films and NPs such as gold (Au), silver (Ag), and copper (Cu) over the graphene layer and the extensive role of structural defects. However, most of the experimental results on the SERS extensively present defective graphene-Au (DGR-Au) ultrathin films before and after rapid thermal annealing (RTA) in the current work. We have estimated the contribution of SERS and LSPR in each case before and after RTA of all the DGR-Au hybrids comparatively. A systematic study on TM NPs' interaction with graphene was carried out from wavelength-dependent Raman spectra in the presence and absence of structural defects in graphene and the effect of RTA on the RRS and LSPR absorption characteristics in each case. FDTD calculations have shown the enhancement of the electric field in the presence of graphene in the DGR-Au hybrid sample. Further, we demonstrate the physical functionalization of graphene with TM NPs from high-resolution transmission electron microscopy (HRTEM) and spatial distribution of micro-Raman mappings. Excitation wavelength-dependent Raman spectroscopy studies reveal that the 632.8 nm laser excitation causes the resonance of Raman features before and after the RTA process as compared to the other visible wavelengths (488 and 514.5 nm), especially in the case of DGR-Au. A significantly stronger LSPR absorption was observed after the RTA process from the graphene-TM hybrid system. Further, DGR-Au plasmonic hybrids exhibit an efficient SERS platform to detect FL and R6G visible fluorescent dye molecules, which show an outstanding performance of Raman signal enhancement of up to $\sim 10^8$ up to nanomolar-level detection capability. This kind of graphene-TM hybrid is a very good candidate for enhanced photocatalytic, biosensor, and optoelectronic applications.

2. EXPERIMENTAL SECTION

2.1. Synthesis of Graphene. We synthesized a monolayer and a few layers of graphene by using an in-house developed catalytic chemical vapor deposition (CVD) system on a Cu foil of 25 μm thickness (Alfa-Aesar). The full details of the sample preparation of the graphene growth and clean transfer of graphene are explained in the previously reported works.[8,10] At first, the Cu foil was inserted into a quartz chamber and flushed with argon gas for 5 min. Then, the chamber was pumped down to a base vacuum of 4×10^{-4} mbar, and the temperature was increased to 1000 °C (growth temperature of graphene) at the rate of 25 °C min^{-1} using a horizontal muffle furnace (Indfur, India). The Cu substrate was preannealed at the same temperature in a reduced environment by flowing 200 sccm (standard cubic centimeters per minute) H_2 gas for 30 min to avoid oxidation of the Cu surface. The final reaction was

https://doi.org/10.1021/acsomega.2c07706
ACS Omega 2023, 8, 4344−4356

carried out by a controlled flow of CH_4 ~18 sccm and H_2 ~200 sccm for 30 min at a temperature of 1000 °C and a pressure of 4.0 mbar. Because graphene was deposited on both sides of the Cu foil, the bottom layer was removed by diamond polishing. The graphene layer on top of the Cu foil was transferred onto the Si/SiO_2 substrate by a conventional wet transfer technique.[14] In this process, poly(methyl methacrylate) (PMMA)/toluene was spin-coated on graphene/Cu, and the underlying Cu was etched in an aqueous $Fe(NO_3)_3$ etchant solution. PMMA/graphene, floating on the etchant solution, was rinsed in deionized water a few times until the PMMA and metal impurities were removed. Then, it was scooped and transferred onto Si/SiO_2 and quartz substrates as shown in Figure 1a.

2.2. H_2 Annealing of Graphene. Achieving high-quality graphene without wrinkles, folds, and surface corrugation is one of the challenging tasks while transferring it from a Cu foil to a required substrate. Although wet transfer is a standard protocol, there are still leftover impurities such as PMMA and catalyst NPs along with oxide traces that are present on the graphene substrate. To remove these impurities from the graphene on the Si/SiO_2 and TEM grid, these samples were annealed in a H_2 atmosphere. Initially, the samples were taken in a quartz boat and kept in a tubular chamber. First, the chamber was pumped down to a base vacuum of 10^{-5} mbar followed by ramping of the temperature up to 400 °C. The graphene annealing was performed under a H_2 gas environment for 2 h. The annealing parameters were chosen as optimum to achieve clean graphene without residual impurities on the graphene surface.[15] The degree of improvement in the crystallinity and spatial homogeneity of graphene layers was confirmed by Raman spectra and Raman mapping in each case before and after RTA, respectively. These samples were further studied for the physical functionalization with metals such as gold (Au), silver (Ag), and copper (Cu).

2.3. Surface Modification of Graphene by TM Films. Next, ultrathin films of TM (Au, Ag, and Cu) films were deposited on the graphene layer by a radiofrequency (RF) magnetron sputtering process with an RF power < 5 W. Figure 1b shows the deposition of the Au film on a defective graphene layer (DGR-Au). TM films were deposited in a controlled manner for 30 s at a deposition rate of 0.8 Å/s. All the TM films were deposited on different substrates (Si/SiO_2/graphene, quartz/graphene, graphene transferred onto a TEM Cu grid). The details of the sample preparation and sample codes are described in Table T1 (see Supporting Information). Note that the high-purity TM targets (99.999%) were used for the sputter deposition.

2.4. Rapid Thermal Annealing of TM Films. The TM sputtered graphene substrates were subjected to rapid thermal annealing (RTA) to make the TM NPs. Figure 1c represents a schematic of the defective graphene Au NP hybrid 2D material after the RTA process. Prior to the RTA process of the DGR-TM film substrate, we have done the RTA of the TM films on SiO_2 substrates at three sets of temperatures to optimize the size of the TM NPs. We have shown the temperature-dependent size evolution of the RTA processed Au NPs at three different temperatures of 580, 600, and 650 °C for a duration of 3 min in an Ar gas atmosphere in the Supporting Information Figure S1, and the corresponding E-field enhancement is mapped using the FDTD simulation software. The TM NPs were found to be uniform in size (~20 nm) and better controlled at 600 °C. The size distribution of Au nanoislands was estimated from the histogram as shown in the inset of Figure S1. Further sample preparation of DGR-TM hybrids using RTA processing was carried out at 600 °C to elucidate the resonance effects from these DGR-TM plasmonic hybrid structures in the following sections.

2.5. Characterization Tools. Micro-Raman measurements were performed with a high-resolution spectrometer (Horiba, Lab Ram HR), with excitation wavelengths (λ_{ex}) of 488, 514.5 (Ar^+ ion laser), and 632.8 nm (He−Ne laser). The excitation source was focused with 100× objective lens, spot size of 2 μm, and laser power of 1 mW to avoid heating and damage to the sample, and the signal was collected by a CCD in a backscattering geometry sent through a multimode fiber grating of 1800 grooves mm^{-1}. Raman mapping images were acquired using a high-resolution Raman spectrometer from Renishaw (inVia) with a spatial resolution of 100 × 600 nm using a streamline imaging facility having a large area coverage (10 × 10 μm^2). AFM measurements were carried out with a Nanosurf instrument. The measurements were obtained in dynamic mode and processed with the Gwyddion software. Field emission scanning electron microscopy (FESEM) (Sigma, Zeiss, operating voltage 0.5−30 kV) imaging using an in-lens detector and HRTEM (JEOL-2100 operated at 200 kV). LSPR absorption from defective graphene-TM PNSs coated on the quartz substrates was recorded by a commercial spectrophotometer (Perkin Elmer UV Win Lab, UV-3101PC), which covers a wide range of wavelength from UV−vis−NIR.

2.6. Fabrication of Defective Graphene and Defective Graphene-Au Plasmonic Hybrid SERS Sensors. At first, the organic dye molecules (R6G and FL) were deposited onto SiO_2 and quartz substrates by dipping in an aqueous dye solution of 10 mL with a dye concentration of 10^{-8} and 10^{-9} M. DGR and DGR-Au SERS substrates were soaked in the dye solution for 1 h and dried in a vacuum oven at ~100 °C for 10 min. A schematic representation of defective DGR-Au NP plasmonic hybrid SERS sensors is shown in Figure 1d. Note that all the samples were prepared on SiO_2 and quartz substrates. The SERS effect of DGR and DGR-Au was estimated from the enhancement of the Raman features of dye molecules in the range of 600−1800 cm^{-1}.

2.7. Spectral Data Analysis. Raman spectral lines of defective and defect-free graphene along with the DGR-TM PNSs at different excitation wavelengths were fitted by Lorentzian line shapes and peak fitting using the Peakfit software with peak parameters as free variables. The best fit was obtained by a large number of iterations.

2.8. Finite Domain Time Difference (FDTD) Calculations. Maxwell's equation system is solved in the time-domain on a grid using a mathematical technique called finite domain time difference (FDTD), which computes the field distribution.[16−18] To analyze the electromagnetic (EM) fields in the gap between the suggested graphene and TM PNS hybrid structure or to study the plasmonic gap mode, FDTD calculations were carried out using the Lumerical FDTD solution software. The proposed design of the SERS-active substrate is based on gold (in the *XY* plane) on a thin layer of graphene, using Si/SiO_2 as a substrate, as illustrated in Figure 1. Surface plasmon polaritons (SPPs) are stimulated at the Au-graphene/Au-air contact, coupling incoming radiation into SPPs and subsequently enhancing the electric field at the interface. The shape of the plasmonic structure, frequency of the incident light, effective refractive index of the pattern, and polarization of the incident light affect how much enhance-

https://doi.org/10.1021/acsomega.2c07706
ACS Omega 2023, 8, 4344−4356

ment occurs.[19] The material characteristics employed in the current investigation for the Si/SiO_2 substrate were the same as those provided by Palik,[20] those used for the gold were the same as those provided by Johnson and Christie,[21] and the material of Falkovsky and Pershoguba was taken to be graphene.[22] Perfectly matched layer (PML) boundary conditions were chosen for the Y and Z directions, and periodic boundary conditions were chosen for the X direction. The number of PML layers in the current investigation was set at 16. The mesh was selected to be 0.21 nm in size conformal. The simulation temperature was held constant at 300 K, whereas the simulation time was held constant at 1000 fs. To mimic a light source with a wavelength ranging from 300 to 1100 nm, a plane-wave source was used.

3. RESULTS AND DISCUSSION

Characteristic Raman features of GR and DGR were recorded using different visible laser excitation wavelengths, such as 632.8, 514.5, and 488 nm. The excitation wavelength-dependent Raman characteristics are shown in Figure 2, which clearly distinguishes the structural quality and the presence of intrinsic defects on GR and DGR, respectively. Figure 2a represents the Raman fingerprints of GR recorded at 514.5 nm laser excitation, which shows sharp G and 2D bands

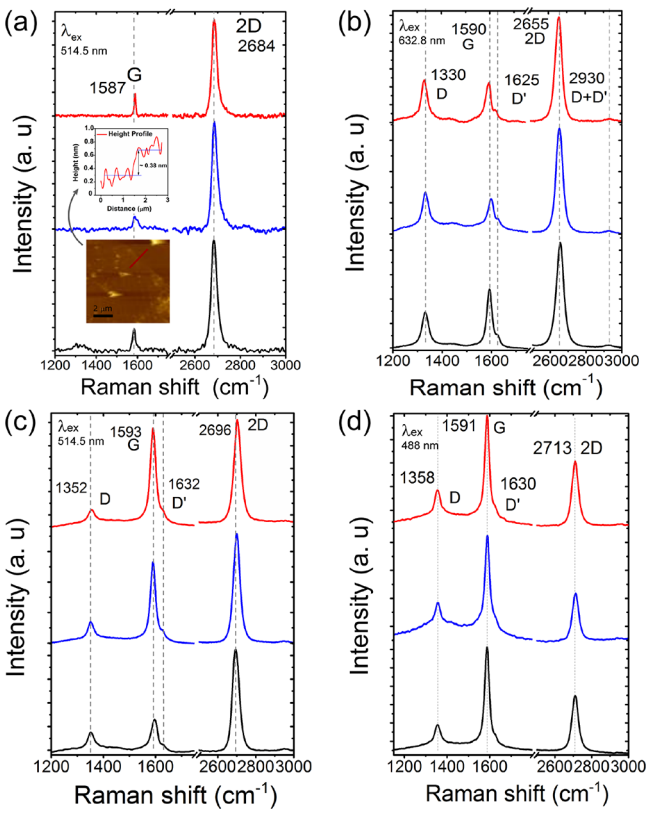

Figure 2. Excitation wavelength (λ_{ex})-dependent Raman features of defect-free and defective graphene: (a) Raman spectra of defect-free graphene measured at different locations with λ_{ex} = 514.5 nm showing sharp symmetric G and 2D bands implying the local distribution of sp^2 hybridized carbon atoms without any significant intrinsic defects and disorder on a monolayer graphene. Note that the inset shows an AFM image of the monolayer graphene and corresponding line profile. (b–d) Raman spectral features (D, G, D′, 2D, and D + D′ bands) of defective CVD graphene, which are collected with λ_{ex} = 632.8, 514.5, and 488 nm, respectively.

with full width at half-maxima (FWHM) ~35 cm^{-1}. The intensity ratio I_{2D}/I_G ~4 signifies the perfect sp^2 crystallinity without any point or extended defects on GR.[10,11] Note that these different spectra in Figure 2 correspond to different scanning locations to assess the homogeneity of the layer. In addition, the inset in Figure 2a represents the AFM image and line profile of the graphene layer on the SiO_2 substrate, and corresponding Raman spectra are shown in the Supporting Information Figure S2. From the Raman plot, we found that I_G/I_{2D} is ~0.302 (less than 0.5), which is strong evidence of the monolayer graphene. For further verification, we conducted AFM experiments, where we found that the thickness of the graphene layer is approximately 0.38 nm, which also confirms the evidence of monolayer graphene. Excitation wavelength-dependent Raman line shape features of DGR are shown in Figure 2b–d that are recorded at 632.8, 514.5, and 488 nm, respectively. The prominent Raman spectral features that are significant for the structural evolution of graphene layers are D, G, D′, 2D, and D + D′ bands as shown in Figure 2. D, D′, 2D, and D + D′ are dispersive in nature, and the physical origin of these double resonance Raman active modes of graphene is well understood in the literature.[23,24] On the other hand, the graphitic G band at 1587 cm^{-1} is a nondispersive characteristic Raman mode, which arises from the sp^2 hybridized carbon from the in-plane stretching of C–C covalent bonds of the graphene. Note that there is a blueshift in the G band and 2D band in the DGR sample at each excitation wavelength, as seen from Figure 2b–d, which might be due to the presence of in-plane defects within the very less interdefect distance and marginally due to the induced lattice strain over the basal plane of graphene after wet transfer on the SiO_2 substrate.[8] The considerable asymmetry and broadening in the line shape of the G-band signify the lattice distortions due to disorder or introduction of foreign atoms into the sp^2 carbon lattice (doping).[8,9,18] Lorentzian line shape parameters such as FWHM, I_D/I_G, and I_{2D}/I_G from peak fitting of these bands are very important to estimate the structural evolution when the graphene layer is functionalized with the suitable nanomaterials with 488 nm laser excitation. The intensity of the 2D band is noticeably less as compared with the others for both DGR and GR (see Figure 2d). The spatial distribution of intrinsic defects and layer uniformity was estimated after the RTA annealing of the DGR sample. In addition, we have shown the Raman mapping image of the DGR sample after the RTA annealing in the Supporting Information (Figure S3). Note that the Raman mapping image was recorded within a frame size of 6 × 6 μm^2 area. (The Raman features of pristine graphene and Au functionalized graphene after RTA treatment show the identical line shapes in terms of the D, G, and 2D bands and other low-frequency Raman modes in the sample.) However, because of the CVD catalyst, metal particles present after PMMA transfer might lead to the local defect and inhomogeneity of the graphene layer on the SiO_2 substrate. After Au deposition, there is not much enhancement in terms of the D band; however, there was an increase in the peak broadening without any peak shifts says about the lattice strain due to the formation of Au NPs after the RTA annealing process, which will be discussed in the next section.

3.1. Optimization of the Transition Metal Layer on Graphene.

At first, for controlled physical functionalization of graphene with TM clusters using RF magnetron sputtering and to minimize the degree of disorder during the sputtering

https://doi.org/10.1021/acsomega.2c07706
ACS Omega 2023, 8, 4344–4356

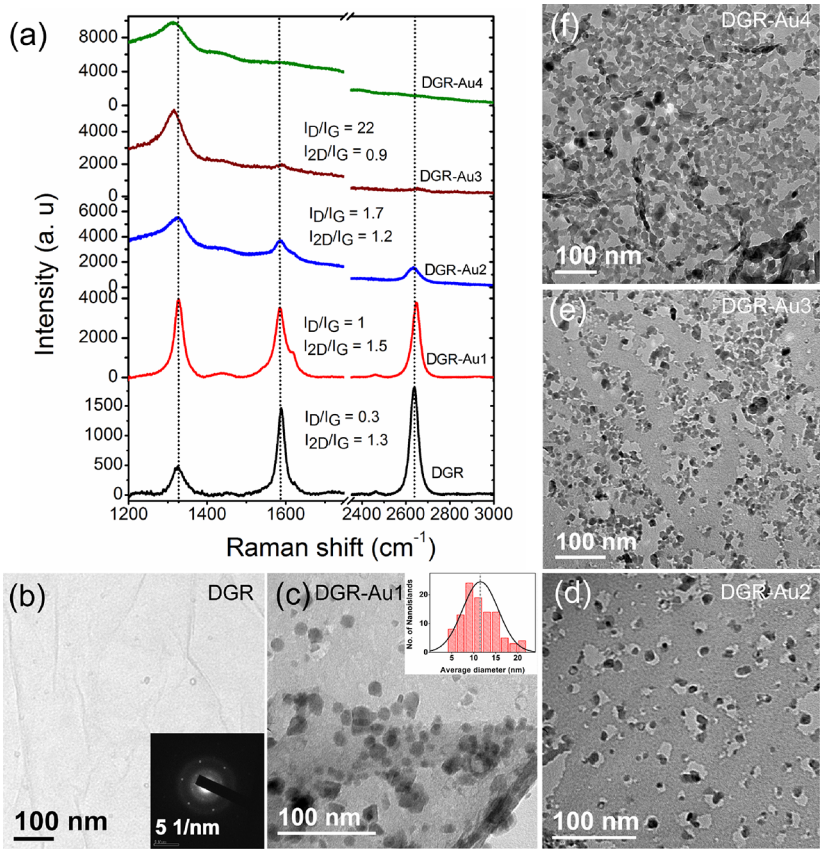

Figure 3. (a) Raman line shape evolution and (b–f) TEM surface morphology of the DGR-Au plasmonic hybrids prepared for different deposition times corresponding to DGR-Au1 (30 s), DGR-Au2 (60 s), DGR-Au3 (120 s), and DGR-Au4 (180 s). Note that the inset of panel c shows the Gaussian size distribution of Au nanoislands statistically estimated with respect to the area of the image.

process, we performed controlled Au deposition on graphene at different time durations and optimized the thickness of Au layer such that it does not deteriorate the sp^2 crystallinity of graphene. The Au film was deposited on the graphene substrates for deposition times of 30, 60, 120, and 180 s. The complete details of the samples are shown in Table T1. Figure 3 represents the Raman line shape features in DGR-Au plasmonic hybrids for different deposition times and the surface morphology as studied by HRTEM imaging of suspended graphene and Au islands. Note that the Au film coated after the duration of 30 s is coded as DGR-Au. It is worth seeing to know that there is a formation of vacancy defects followed by Au NP encapsulation/dewetting taking place over the basal plane of graphene through defect sites (see Figure 3). It is interesting to note that the Au clusters are separated by some distance, and it spreads across the whole DGR substrate. It is most likely that the interaction of Au clusters is initiated from the vacancy defects that are formed during the RF sputtering process and then defect-mediated covalent functionalization of graphene with Au clusters takes place on the graphene plane (see Figure 3). At higher deposition times (>120 s), the 2D band becomes weak and the line shape of the D band becomes broad in the Raman spectra, partly as a result of the damage of the graphene layer. Note that we calculated the defect density (n_D) and interdefect distance (L_D) in our DGR samples using the empirical relations used in the previously reported work.[8,25] L_D and n_D were calculated from the Raman line shape analysis as a function of I_D/I_G and λ_{ex} in each case as shown in Table T1. It is found that the enhanced n_D was observed in the case of DGR-Au3, whereas in DGR-Au4 (see Figure 2), the graphitic structure of DGR completely deteriorated. The result of the HRTEM image analysis is consistent with the Raman line shape. On the basis of the experimental observations, we found that 30–60 s is the optimum deposition time to achieve controlled DGR-Au plasmonic hybrids using our sputtering system without losing sp^2 crystallinity. Note that the further studies are implemented with the above-mentioned deposition parameters for the fabrication of graphene plasmonic substrates for efficient SERS sensors. Further FDTD calculations are shown in the Supporting Information. Figure S4 shows that the sample DGR-Au (Figure 3c) has the highest E-field enhancement as compared to DGR-Au at higher deposition rates (Figure 3d–f) at 514.5 nm excitation wavelength due to small gapping, agglomeration of Au NPs, and hotspots that occurred to trap light, which lead to better electric field distribution.

3.2. Micro-Raman Studies. To understand the role of defects in the functionalization of DGR with TM NPs, we performed Raman imaging of graphene samples after physical functionalization. Figure 4 illustrates the areal intensity maps of characteristic Raman modes of D and G and the ratio of intensity I_D/I_G in DGR-Au and DGR-Ag plasmonic hybrids in the scanning area of 5 × 5 and 10 × 10 μm^2, respectively. Note that the intensity scale bars are separately shown for better visibility of each band. The position and layer-dependent Raman spectra of the DGR-Cu plasmonic hybrid and corresponding FESEM images are shown in the Supporting

https://doi.org/10.1021/acsomega.2c07706
ACS Omega 2023, 8, 4344–4356

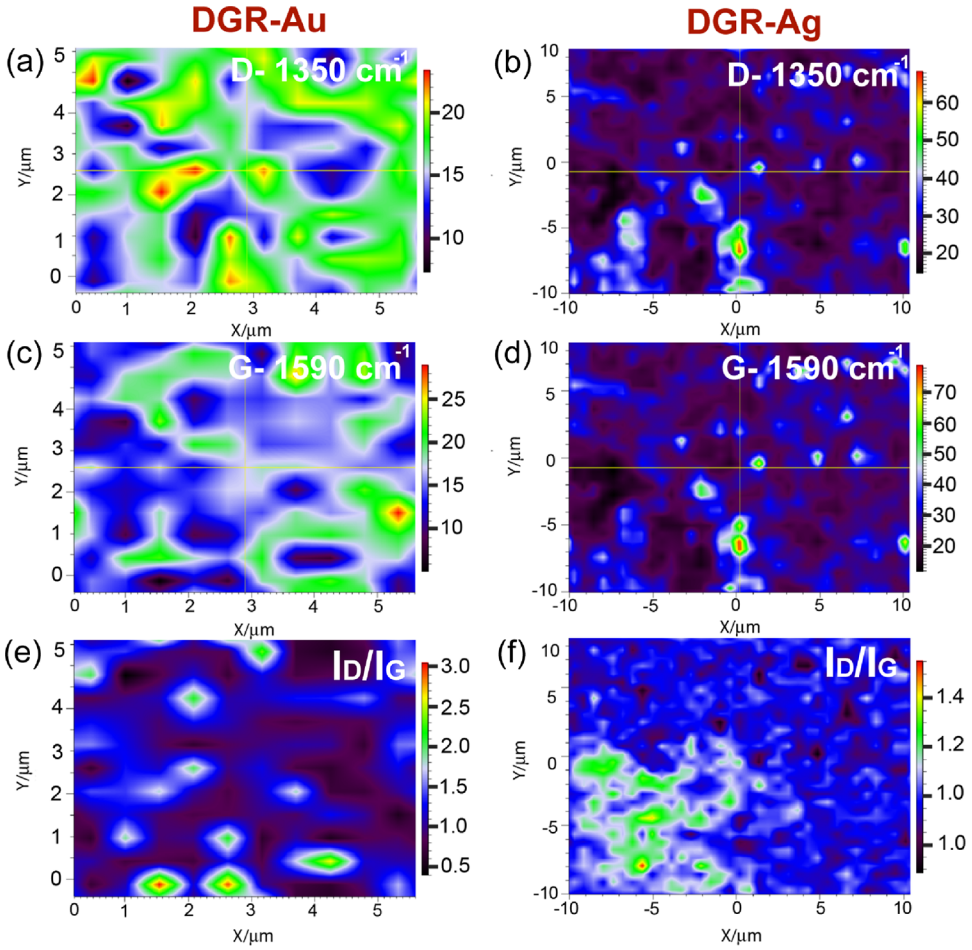

Figure 4. Spatial Raman mapping images showing the Au and Ag layer over the defective graphene: The Raman mappings are shown for the (a, b) D band, (c, d) G band, and (e, f) integrated intensity ratio (I_D/I_G) in DGR-Au and DGR-Ag samples, respectively. Note that the scanning area of the Raman mappings is 5 × 5 μm^2 for DGR-Au and 10 × 10 μm^2 for DGR-Ag. [Panels a, c, and e are reprinted with permission from the Catalysis Science and Technology, copyright (2016), Royal Society of Chemistry, *Catal. Sci. Technol.*, **2016**, *6*, 7101−7112].

Information Figure S5. Figure 4e,f shows the relative areal intensity ratio maps of the D and G bands in DGR-Au and DGR-Ag, respectively, which constitute evidence for the sp^2 crystallinity with a large coverage of SLG and BLG that are covered with TM NPs at various points and extended defects in the graphene layer. Figure 4e,f depicts the areal intensity variations of the D and G bands from the I_D/I_G map, which signify the TM NPs' coverage on the DGR substrate. The red and green color contrast in the I_D/I_G Raman maps is significant for the Au and Ag clustering process. We have shown the excitation wavelength-dependent Raman line features of DGR-Cu hybrids in Figure S4, which signify the enhanced Raman signal; however, it is as poor as SERS sensors, which may be due to the fact that Cu can be easily oxidized, and it leads to the poor Raman activity of the graphene-plasmonic structure as compared to Au and Ag films/NPs. Further, it is evident from Figure S4c,d that shows the morphology of diffusion of Cu over defective graphene through edges. Present case the initial sample grain size is too small and gold nucleation takes place at the edge sites of graphene grains further basal plane coverage at the higher deposition rates leads to the deterioration of the D band, D and G bands exist at the moderate deposition of gold using RF magnetron sputtering. Note that the characteristic Raman signatures of GR and DGR were discussed in the previous section. Figure S6 (Supporting Information) represents an evolution of Raman fingerprints of pristine and Au functionalized DGR (Figure S5a) and DGR-Au (Figure S5b), and the respective scanning locations are shown in the OM image. Note that both samples were prepared under controlled deposition conditions as discussed in the previous section. The sharp G and 2D bands (I_{2D}/I_G > 2) with a negligible D band signify the perfect sp^2 crystallinity with monolayer coverage of graphene in DGR. The surface modification of Au NPs on DGR gives rise to the appearance of a strong D band and a considerable redshift in the 2D band due to the in-plane lattice strain in the graphene layer, which arises from the coverage of Au NPs. Note that we have not observed any significant shift and change in the FWHM of the G band ($\Delta\omega_G$) after Au deposition, which reveals the covalent interaction of Au NPs with DGR. The sharp D and D′ bands in DGR are significant for the various intrinsic defects (vacancies, line and extended defects, etc.) on the graphene layer. The site-selective defect-mediated interaction of Au NPs on the DGR layer was clearly revealed from the strongly enhanced intensity of the D, D′, and D + D′ bands as compared to that of the G and 2D bands.[5] We will discuss more details of the same in a later section along with its characterization results. Note that, after functionalization, both G and 2D bands show a redshift, which signifies the p-doping of GR.[26] A new Raman band at 1430 cm^{-1} represents the interaction of Au NPs at the edge

https://doi.org/10.1021/acsomega.2c07706
ACS Omega 2023, 8, 4344−4356

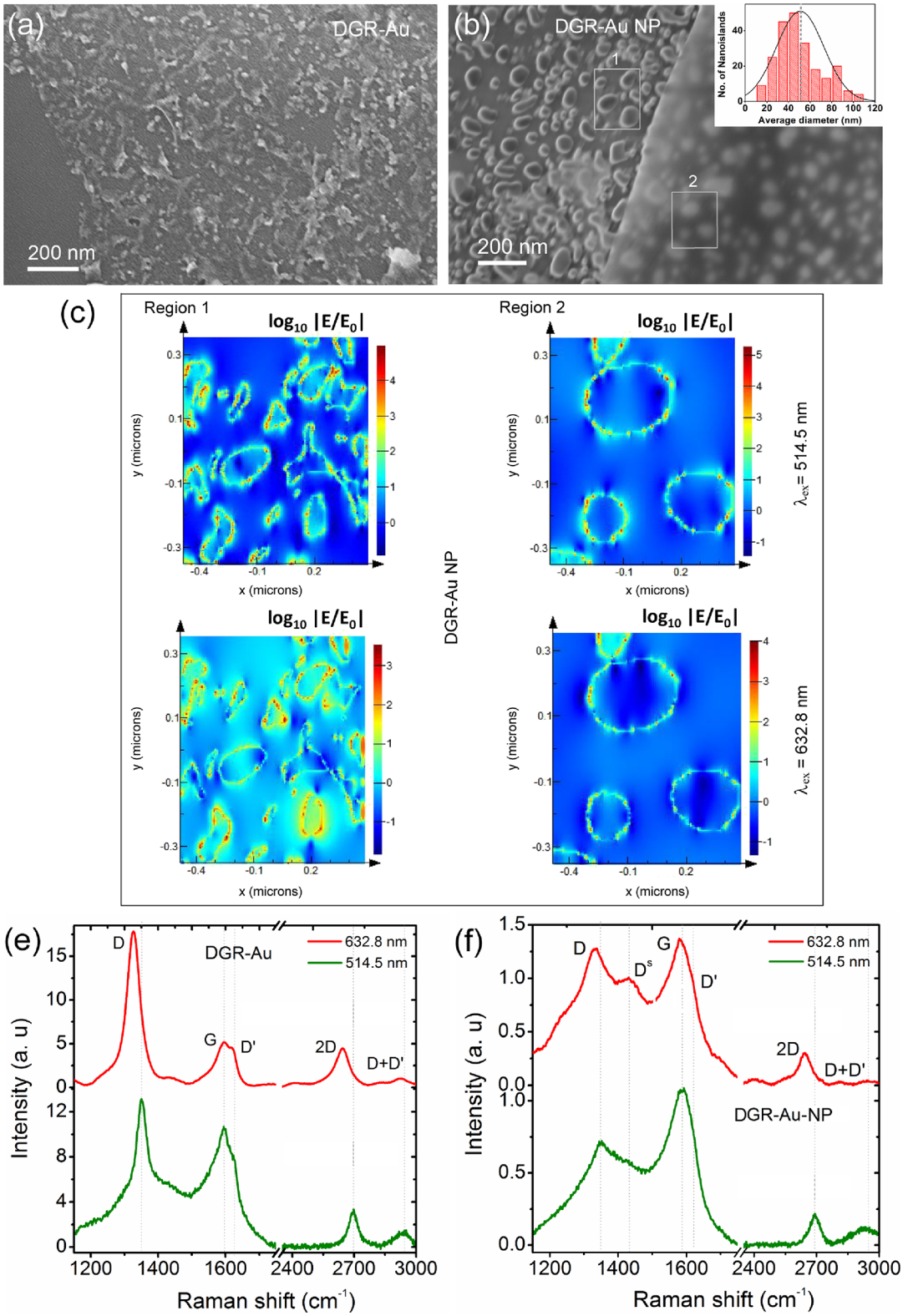

Figure 5. (a) FESEM image of pristine DGR-Au and (b) RTA-treated DGR-Au on the Si/SiO_2 substrate (DGR-Au NP). FDTD-simulated electric field mappings of (c) DGR-Au NP extracted from regions 1 and 2 as shown in the FESEM image. Note that the $\log_{10}|E/E_0|$ is mapped at 514.5 and 632.8 nm excitation wavelength (λ_{ex}). λ_{ex}-dependent Raman features of Au functionalized defective graphene (e) before RTA and (f) after RTA treatment, measured at λ_{ex} = 514.5 and 632.8 nm. Note that the inset of panel b shows the Gaussian size distribution of Au nanoparticles statistically estimated with respect to the area of the image.

sites of the graphene layer.[27] Raman features of DGR were equally enhanced after Au functionalization, whereas in DGR, defect-related Raman modes are enhanced significantly, which are due to the strong bonding of Au clusters at defect sites that creates a lattice distortion on the basal plane of graphene.

https://doi.org/10.1021/acsomega.2c07706
ACS Omega 2023, 8, 4344−4356

3.3. Effect of RTA Treatment. Morphological features of GR-TM hybrids before and after RTA treatment were investigated by FESEM and HRTEM measurements as shown in Figure 5. Figure 5a,b shows the FESEM images of DGR-Au hybrids before and after RTA treatment. The inset of Figure 5b shows the size distribution of Au NPs after the RTA process, which are fabricated on the Si/SiO_2 substrate. The inset of Figure 5b represents the Gaussian size distribution of Au NPs after the RTA process. The size of Au NPs is almost doubled as compared to the grain size of the Au film previously discussed (see Figure 3c). Morphological features of the graphene layer coated with Ag and Cu films are shown in the Supporting Information Figure S7. It is worth seeing to observe the identical physical characteristics as identified in the case of the Au layer. The inset of Figure 5b shows the shape evolution of Au NPs on the SiO_2 substrate for comparison with the graphene substrate after RTA treatment. Note that DGR-Au (Figure S7a), DGR-Ag (Figure S7b), and DGR-Cu (Figure S7c) hybrids were prepared on a TEM Cu grid. Figure 5c presents the simulated electric field distribution between spherical Au nanoparticles in the $x-y$ plane of region 1 and region 2 corresponding to the absence and presence of graphene underneath them, respectively. Note that the E-field distribution is shown at 514.5 and 632.8 nm laser excitations. Interestingly, the average size of Au NPs is found to be ∼50 nm, corresponding to the grain size of the roughened Au-surface on defective graphene after the RTA process as analyzed using FESEM images (illustrated in Figure 5b). It is well acknowledged that EM plays a key role in enhancing the Raman signals discussed before, which principally results from the excitation of the LSPR. The DGR-Au generates a strong electric field, which may lead to improvements of 4 to 11 orders in magnitude. In the present case, at 514.5 nm laser excitation, the highest E-field enhancement of the order of ∼5 (see Figure 5c) is shown, which is a very close SPR absorption peak of Au NPs. Utilizing the widely available Lumerical software, we have done FDTD simulations of the DGR-Au and DGR-Au NP on the Si/SiO_2 substrate.[16−19] In accordance with the grain size of the annealed DGR-Au surface and as examined using FESEM and TEM images, the simulated electric field distribution between DGR-Au nanoparticles in the $x-y$ plane is shown in the Supporting Information Figure S8b (illustrated in Figures 3 and 5). The color bar from blue to red shows the electric field's increasing intensity. We have used further FDTD analysis that reveals that the DGR-Au hybrid after the RTA annealing process as shown in Figure 5b has more E-field enhancement in comparison to the DGR-Au hybrid before treatment (Figure 5a) due to the presence of sharp edges and hotspots around the Au NPs (see Supporting Information Figure S8). In Figure 5c, it is clearly shown that hotspots can occur between two Au nanoparticles. Following treatment, which improved the Raman signal, the greatest electric field for DGR-Au nanoparticles was detected (10^4-10^5). When Au grains are grown on the surface of the DGR over a Si/SiO_2 substrate with the proper gap between the grains, an electric field is produced that has a high intensity as depicted in Figure S8b. The strongest electric field is observed for Au nanoparticles on DGR size ∼50 nm and gap = 2.5 nm leading to Raman signal enhancement. It is generally agreed that the formation of localized collective oscillations of conduction electrons results in SERS enhancement. The resonance frequency primarily depends on the size, shape, and uniformity of SERS nanoparticles, which can directly affect the distribution of the electric field and consequently affect SERS enhancement. As a result, it is found that the experimental results of the graphene and DGR-Au plasmonic hybrids for SERS applications are in good agreement with the corresponding theoretical analysis based on FDTD E-field calculations that are described here. It indicates that the TM NPs are present at the defect sites of graphene, more prominently at the edge defects. Raman analysis shows that the as-synthesized graphene contains a large number of defects on the basal plane and imperfect edges, as evident from the D′ band in the pristine graphene. After Au deposition, it was found that the Au islands were formed not only at the edges (see Figure 5b) but also at the defect sites on the basal plane of graphene. In all the samples, the size of TM NPs varies in the range of 5 to 10 nm with an oval shape. We found a considerable increase in vacancy defects after TM functionalization of DGR TM NPs. Interestingly, we observed a major enhancement in the intensity of D and D′ bands after Au deposition as compared to that of G and 2D bands, as discussed in the previous section. The effect of RTA treatment on Raman features of DGR-Au plasmonic hybrids is demonstrated in Figure 5e,f measured at two excitation wavelengths (632.8 and 514.5 nm). With the Au layer on graphene before and after RTA treatment, the high ratio of I_D/I_G and corresponding low L_D are significant for the Au clustering at the intrinsic defect sites formed on the graphene surface.[10,28] It is well known that except for the G band, all second-order double resonance Raman modes D, D′, 2D, D + D′, and 2D′ including weak combinational modes between 1700 and 2300 cm^{-1} of graphene are strongly dispersive in nature with respect to λ_{ex}.[29,30] We carried out the Raman studies on DGR and DGR-Au with λ_{ex} = 632.8 nm as strong resonance Raman features were observed in DGR sample at this wavelength. Figure 5e,f depicts the comparison of Raman features of DGR-Au before and after the RTA process at two different laser excitation wavelengths, namely, 514.5 and 632.8 nm. It may be noted that no substantial change in the FWHM ($\Delta\omega_D$) and position of D and D′ bands was observed after the RTA process. It is clear that in DGR-Au at 632.8 nm excitation, the D band intensity is enhanced by a factor of ∼33, whereas the D′ band is enhanced only by a factor of ∼13 as compared to that of DGR. In contrast, the intensities of G, 2D, D + D′, and 2D′ bands are increased only by a factor of ∼5 in DGR-Au. Interestingly, the second-order weak modes are equally enhanced in DGR-Au. In addition, it is found that the FWHM of the 2D band ($\Delta\omega_{2D}$) in DGR-Au is significantly higher (70 cm^{-1}) than that in DGR (43 cm^{-1}). The higher FWHM in DGR-Au may be partly caused by the diffusion of Au atoms into the graphene layer due to the presence of defects.[8] Because of RTA treatment, there is a local diffusion of Au atoms on the graphene plane, which makes the line shape broad for all characteristic Raman bands (see Figure 5e). This is more evident from the HRTEM analysis, as discussed in the supporting section (see Figure S6). During the RTA treatment of the substrate at 600 °C in an Ar atmosphere, Au atoms migrate and segregate at the defect sites to form Au clusters, and dewetting (liquid and solid) may be higher at the pristine graphene-defect-free sites. Indeed, we observe a distinctly different behavior of Au clustering on the Si/SiO_2 substrate and Si/SiO_2/graphene substrates coated with the Au layer during the RTA process (see Figure 5b). Spherical Au nanoparticles are formed in the former case, whereas nonspherical or dumbbell-shaped bigger Au NPs are formed

https://doi.org/10.1021/acsomega.2c07706
ACS Omega 2023, 8, 4344−4356

in the latter case. The dramatic increase in intensity of the D band as compared to that of the G band after Au deposition indicates a SERS enhancement of the Raman intensity caused by preferential clustering of the Au atoms specifically at the defect sites in graphene, whereas in RTA-treated samples, the intensity of Raman features is reduced by a factor of nearly ∼10. Note that identical results are found in the case of DGR-Ag and DGR-Cu hybrids as shown in the Supporting Information (Figure S5). This provides a very important insight on the enhanced localized SPR absorption due to the formation of bigger Au NPs over the graphene plane after RTA treatment. Absorption spectra of DGR-Au before and after RTA treatment confirm the same as discussed in the next section. Wang et al. provided direct evidence of metal doping/clustering at the in-plane defect sites in graphene by in situ aberration-corrected TEM.[28] The stability of the metal clusters was argued on the basis of the high binding energy of the metal-vacancy complex in graphene. Note that some of the Au atoms may diffuse through the graphene[31] and form chemical bonds with carbon atoms of graphene as longer Au−C bonds,[30] and this may be responsible for the dumbbell-shaped Au NPs (see Figure 5b). The shape deformation and larger dimension of the Au NPs clearly indicate that a large number of Au atoms migrate and cluster preferentially at the defect sites, driven by the dewetting behavior of Au on the graphene layer[32] and for energy minimization. FESEM image analysis shows that the areal density of Au NPs in the presence and absence of the graphene layer and the areal density of Au NPs on the Si/SiO_2 substrate are ∼25 and 117 μm^{-2}, respectively. In the presence of the graphene layer, the areal density of Au NPs is reduced by a factor of ∼5. This reduced density of Au NPs on the graphene layer is dictated by the Au thickness and dewetting behavior of graphene and the density of defects in the graphene layer. Interestingly, Raman analysis shows that the average areal density of defects in pristine graphene and the DGR-Au hybrid layer is in the range of 490−860 and 3985−4950 μm^{-2}, respectively. It implies a nearly sixfold increase in defect density after Au deposition by sputtering. On the other hand, the Au NP density is only about 5% of the graphene defect density, which is limited by the thickness of the Au layer deposited.

To support the resonance Raman effect, we performed the absorption measurements of DGR, DGR-Au, DGR-Ag, and DGR-Cu hybrids fabricated on the quartz substrates. Figure 6a,b shows the absorption spectra of DGR-Au and DGR-Ag in comparison with pristine graphene on the quartz substrate. With reference to the experimental results observed for the plasmonic enhancements for the Au NPs on graphene, similar NP structures were modeled and simulated using calculations also shown in Figure 6a,b. Note that the absorption spectra of DGR-Cu including FDTD simulations are shown in the Supporting Information Figure S9. The SPR absorption peaks of Au, Ag, and Cu NP SPR peaks were found at 570, 485, and 445 nm experimentally. The SPR absorption peaks from FDTD calculations are predicted to be 540, 412, and 580 nm for Au, Ag, and Cu theoretically (see Supporting Information SI.1). The key points identified from these data are the stronger SPR absorption peak in DGR-Au and DGR-Ag as compared to that of DGR-Cu and the enhanced peak intensity after RTA treatment. Further, the SPR absorption peak of DGR-Au and DGR-Ag is stronger by a factor of ∼5 after the RTA process, and it shows a redshift, which may be due to the strong covalent functionalization of Au with defective

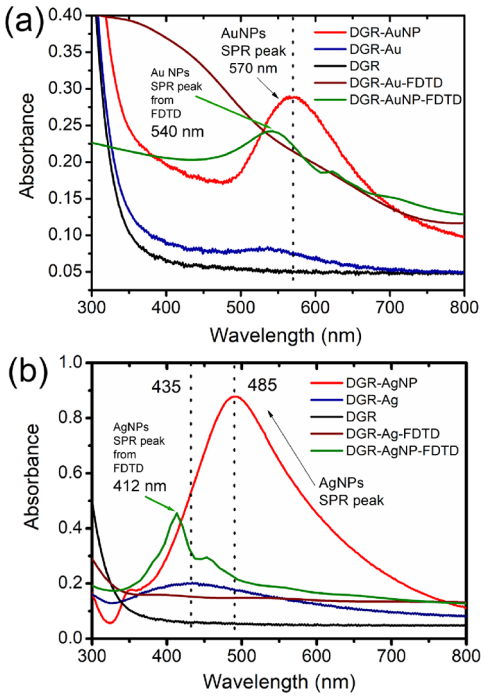

Figure 6. LSPR absorption spectra of defective graphene-TM Hybrids: (a) DGR-Au and (b) DGR-Ag plasmonic hybrid based on the experiment and FDTD simulation, in comparison to a pristine defective graphene layer.

graphene. Note that after RTA treatment, we observed a reduction in the SERS signal as discussed in the previous section. The size and shape of the Au NPs decide the amount of SPR enhancement. However, there is a slight variation in the SPR peak position in case of both DGR-Au and DGR-Ag hybrids for simulated and experimental results (see Figure 6a,b). These variations may be due to the randomness of the synthesized plasmonic NPs in the current experiments, whereas the simulated NPs have a high degree of symmetricity. Also, the synthesized NPs vary slightly in size and shape, but in the simulation, the average size and shape are considered. Because of the small size of the TM NPs formed here limited by the thickness of the TM layer, SPR enhancement was about only 1 order of magnitude. Note that the SPR absorption-induced reduction in Raman intensity is insignificant before the RTA treatment because the surface coverage of the Au NPs on the graphene is much smaller than the maximum possible coverage.[33] One may expect aggregation and bonding of the respective atoms/molecules covalently at the defect sites of graphene, which reduce the SERS signal and increase the SPR absorption after RTA. The broadening of D, G, D′, and 2D bands (see Figure 6e,f) in the DGR-AuNP spectrum thus confirms the strong interaction of Au NPs at the in-plane defects and edges.

3.4. SERS Studies on Graphene and Graphene-Au Plasmonic Hybrids. Prior to the SERS measurements from the dye molecules, pristine and Au functionalized graphene samples were characterized from the micro-Raman spectroscopy, as discussed in the previous section. Figure 7a,b represents the SERS spectra of FL and R6G collected on the pristine DGR, DGR-Au, and Au-coated SiO_2 substrates, respectively. Note that the SERS spectra were acquired for 10^{-8} and 10^{-9} M concentrations and denoted by numbers "1" and "2" in each sample, respectively. Raman spectra show the

https://doi.org/10.1021/acsomega.2c07706
ACS Omega 2023, 8, 4344−4356

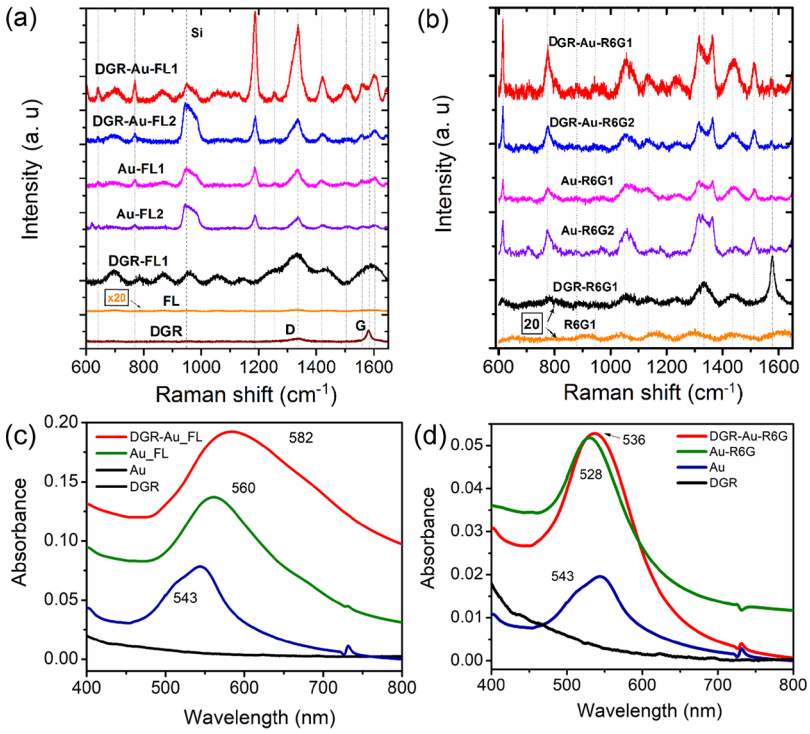

Figure 7. A comparison of Raman enhancements from DGR, DGR-Au, and Au SERS substrates after subtraction of fluorescent background for (a) Fluorescein (FL) and (b) Rhodamine 6G (R6G) dye molecules. The Raman spectra of defective graphene are also shown in panel a for comparison. Note that FL1/FL2 and R6G1/R6G2 correspond to the concentration of dye of 10^{-8} and 10^{-9} M, respectively. Optical absorption spectra from (c) FL and (d) R6G dye molecules (10^{-8} M) coated on Au and DGR-Au deposited quartz substrates. For comparison, spectra of DGR and Au are also shown in each case.

symmetry vibrational modes of the dye molecules, which are present in the range of 600−1800 cm^{-1}. The Raman signals at 1187, 1336, 1421, 1505, 1560, 1603, and 1641 cm^{-1} are very strong in case of FL on the DGR-Au SERS substrate, and the weak Raman bands at 614, 643, and 772 cm^{-1} are still distinguishable on the monolayer DGR-Au substrate, whereas on Au and graphene substrates, these bands are weak. In case of R6G, we found the strong Raman signals at 614, 777, 1314, 1363, 1512, and 1650 cm^{-1}. For both dye molecules, we found a fluorescence background on the SiO_2 substrate. However, the DGR and DGR-Au substrates show fluorescence quenching for both dye molecules.[34] We estimated the Raman enhancement in each case from the SERS spectra after subtraction of the fluorescence background of graphene and Au. The intensity of each spectrum was normalized with respect to the 1188 and 614 cm^{-1} bands in DGR-Au-FL1 and DGR-Au-R6G1 samples, respectively. It clearly depicts the enhanced Raman signal from the DGR-Au substrates for both dye molecules.

We studied the effect of adsorption of the molecules on the SPR absorption spectra of the DGR-Au plasmonic hybrids in comparison to the pristine samples. Figure 7c,d represents the SPR absorption spectra of DGR and DGR-Au before and after soaking of dye molecules with a comparison with the pristine graphene sample on the quartz substrate. Note that the absorption spectrum of pristine Au is also shown for the comparison. The SPR absorption peaks for FL on Au and DGR-Au substrates are found at 560 and 582 nm, whereas those of R6G are found at 528 and 536 nm, respectively. The relative intensity of SPR absorption from FL dye molecules coated on DGR-Au substrates is higher than that of the Au substrate by a factor of 2, whereas in the case of R6G, both DGR-Au and Au show an almost identical intensity of absorption (see Figure 7c,d). We found that there are a redshift (582 nm) and a blueshift (543 nm) of SPR band in FL and R6G, respectively. The SPR absorption enhancement and shift in SPR peak in the DGR-Au case may be due to the enhanced charge transfer from the underlying graphene to Au and dye molecules due to the strong interaction of graphene with Au NPs.[8] Note that the absorption centers of FL and R6G are at 464 and 523 nm, respectively, as shown in the Supporting Information Figure S10. We have estimated the enhancement factors of the common Raman bands observed in the dye molecules as shown in Table 1. It reveals that the dye molecules do not show significant Raman enhancements on pristine graphene as compared to the DGR-Au and Au SERS

Table 1. Summary of the SERS Enhancement Factors for the Selected Raman Bands of FL and R6G Calculated with Respect to the Raman Intensity of Molecule on the Bare SiO_2 Substrate

	Fluorescein (FL)			Rhodamine 6G (R6G)		
	peak (cm^{-1})	DGR-FL1 (10^8)	DGR-Au-FL1 (10^8)	peak (cm^{-1})	DGR-R6G1 (10^8)	DGR-Au-R6G1 (10^8)
1.	643	0.89	*1.64*	614	0.13	*1.8*
2.	771	0.33	0.33	777	0.16	*1.15*
3.	1188	0.36	*1.41*	1050	0.1	0.3
4.	1334	0.59	*1.48*	1312	0.1	0.3
5.	1421	0.69	*1.15*	1362	0.23	*1.05*
6.	1505	0..3	*2.23*	1434	0.07	0.2
7.	1561	0.46	0.56	1512	0.03	0.49
8.	1598	0.49	0.69			
9.	1644	0.54	1.08			

https://doi.org/10.1021/acsomega.2c07706
ACS Omega 2023, 8, 4344−4356

substrates. DGR-Au SERS substrates show superior Raman enhancement of the order of 10.[8] Note that we performed the SERS measurement for all the substrates at two different dyes up to nanomolar concentrations and found a similar behavior. On the basis of the experimental observations, the mechanism of SERS enhancement is discussed below.

3.5. Mechanism of SERS Enhancement. There are numerous experimental and theoretical works on SERS studies that reveal the enhancement mechanism.[3,26,34,35] Normally, the two widely accepted mechanisms are electromagnetic mechanism (EM) and chemical mechanism (CM). In the case of EM, the enhancement of the local electromagnetic field increases the cross section of the Raman scattering. The contribution to the electromagnetic enhancement is primarily due to the surface plasmons excited by the incident light. The enhancement is roughly proportional to $|E|^4$ and can go up to 10^8 or more, where E is the intensity of the electromagnetic field.[34−36] As compared to EM, CM is based on a charge transfer between the molecule and the substrate, and enhancements are usually $10-10^2$. In many cases, the two mechanisms coexist. In the present case, we have observed the Raman enhancement factor in our DGR-Au hybrids in the order of 10^8 based on the recently reported works (see Table 1). The mathematical formulation of SERS enhancement factor is shown in the Supporting Information SI 2. We believe that the Raman enhancement in our samples is contributed by both EM and CM. The former is due to the SPR absorption from the Au NPs on the graphene surface, and the latter is due to the strong $\pi-\pi$ interaction of dye molecules with the inert nature of graphene surface containing strong sp^2 hybridized carbon atoms and covalently functionalized with Au NPs. Ideally, rough metal surfaces like Au, Ag, Cu, etc., show huge Raman enhancements.[22] DGR-Au and Au hybrid substrates are thought to be marginally rough in nature, not as flat as graphene, which may contribute to the EM enhancement. Because Au particles are embedded in defective graphene, it will have a large curvature and absorb a large extent of incident light to produce surface plasmons.

We deposited the dye molecules by pure solution soaking in which the distance between the molecules is expected to be below 0.2 nm so that charge transfer can occur from the graphene-Au to the molecule.[34,36] First, we consider the graphene as a one atom thick and smooth surface without any fluctuations.[34,36] Second, it has high optical transparency (97.7%). Besides, the SPR on graphene is in the frequency range of terahertz rather than the visible range. Based on these considerations, only graphene is not expected to directly support the EM enhancement. On the other hand, Au NPs possess huge SPR absorption in the visible region, as we discussed in the previous section (see Figure 7c,d). Thus, the major enhancement comes from the EM. On the basis of our FDTD calculation, the EM enhancement factor is likely to be $\sim 10^5$, whereas the CM enhancement factor is expected to be $\sim 10^3$. Note that the magnitude of the Raman enhancements reported in the literature is 2−17 times using pristine graphene as a SERS substrate, whereas for the GO-Au and Ag plasmonic hybrids, it is of the order of 10^1-10^2 based on the CM.[34−39] In the present case, EM enhancement of the order of 10^4-10^5 (as revealed from FDTD simulation) and the enhanced charge transfer between the dye molecule and the DGR-Au plasmonic giving rise to a CM of the order of 10^3 give rise to the overall Raman enhancement of the order of 10^8, which is remarkable.

4. CONCLUSIONS

We have fabricated various graphene-TM plasmonic hybrids, such as Au, Ag, and Cu, onto the CVD graphene with defects in it and studied the SERS and SPR effects from the graphene-TM plasmonic hybrids before and after RTA treatment. A quantitative analysis of defects and defect-mediated TM NP interaction of graphene was performed by resonance Raman spectroscopy, LSPR absorption, Raman imaging, and HRTEM from the spatial distribution of TM NPs through the defects on a graphene layer. We implemented the experimental results of graphene and DGR-Au plasmonic hybrids for SERS applications that are in good agreement with the corresponding FDTD E-field calculations presented here. A systematic investigation on enhanced SERS mechanism was performed. Defective graphene and DGR-Au plasmonic hybrids were implemented for the SERS applications and achieved an impressive Raman enhancement in the order of 10^8 with a detection limit down to 10^{-9} M concentration of dye molecules.

■ ASSOCIATED CONTENT

Supporting Information

The Supporting Information is available free of charge at https://pubs.acs.org/doi/10.1021/acsomega.2c07706.

FESEM images of Au NPs on SiO_2 substrates after RTA treatment at three different temperatures of 580, 600, and 650 °C (Figure S1); Raman spectra of a defect-free graphene on the SiO_2 substrate (Figure S2); 3D Raman spectra of RTA annealed defective graphene (Figure S3); FDTD-simulated electric field mappings of TEM images (Figure S4); excitation wavelength-dependent Raman spectra of the DGR-Cu hybrid and FESEM image of DGR-Cu (Figure S5); Raman spectra of the single-layer DGR and DGR-Au hybrid (Figure S6); TEM images of the graphene-TM metal hybrid (Figure S7); FDTD-simulated electric field mappings of DGR-Au and DGR-Au NP hybrids (Figure S8); LSPR absorption spectra of the DGR-Cu hybrid (Figure S9); estimation of the SPR absorption graphene-TM metal hybrid using FDTD simulation (SI1); optical absorption spectra of Fluorescein and Rhodamine 6G molecules (Figure S10); Raman spectral line shape analysis of I_D/I_G and I_{2D}/I_G (Table S1); and calculation of SERS enhancement factor (SI2) (PDF)

■ AUTHOR INFORMATION

Corresponding Authors

Ravi K. Biroju − *Centre for Nanotechnology, Indian Institute of Technology Guwahati, Guwahati, Assam 781039, India; School of Advanced Sciences−Division of Physics, Vellore Institute of Technology, Chennai, Tamil Nadu 600127, India;* Present Address: Centre for Nanodiagnostics of Materials, Faculty of Materials Science and Technology, Slovak University of Technology, Vazovova 5, Bratislava 812 43, Slovakia; orcid.org/0000-0002-4152-7509; Email: ravikumar.biroju@vit.ac.in

Pravat K. Giri − *Centre for Nanotechnology and Department of Physics, Indian Institute of Technology Guwahati, Guwahati, Assam 781039, India;* orcid.org/0000-0003-2020-4249; Email: giri@iitg.ernet.in

https://doi.org/10.1021/acsomega.2c07706
ACS Omega 2023, 8, 4344−4356

Authors

Bhanu Chandra Marepally − *Chaitanya Bharati Institute of Technology, Hyderabad, Telangana 500075, India;* orcid.org/0000-0001-5836-856X

Pariksha Malik − *Nanostech Laboratory, Department of Physics, Indian Institute of Technology Delhi, New Delhi 110016, India;* orcid.org/0000-0001-8008-378X

Soumen Dhara − *School of Applied Sciences, Kalinga Institute of Industrial Technology, Bhubaneswar 751024, India;* orcid.org/0000-0002-4774-3966

Saravanan Gengan − *Department of Chemistry, Saveetha School of Engineering, Saveetha Institute of Medical and Technical Sciences, Saveetha University, Chennai, Tamilnadu 602105, India;* orcid.org/0000-0002-2349-546X

Dipak Maity − *Surface Science and Interface Engineering Group, Tata Institute of Fundamental Research Hyderabad, Hyderabad 500 107, India*

Tharangattu N. Narayanan − *Surface Science and Interface Engineering Group, Tata Institute of Fundamental Research Hyderabad, Hyderabad 500 107, India;* orcid.org/0000-0002-5201-7539

Complete contact information is available at: https://pubs.acs.org/10.1021/acsomega.2c07706

Notes

The authors declare no competing financial interest.

■ ACKNOWLEDGMENTS

We acknowledge the Central Instruments facility, IIT Guwahati, for providing micro-Raman and HRTEM facility to carry out this work. We thank Dr. Sandip Dhara, IGCAR, Kalpakkam, for the support with the Raman mapping data. Dr. Ravi K. Biroju acknowledges the Royal Society of Chemistry (RSC) research fund (Application: R21-4328734833) support to carry out some part of this work. Dr. M. Bhanu Chandra acknowledges the Science and Engineering Research Board (SERB) under a Core Research Grant (CRG/2019/005985).

■ REFERENCES

(1) Grigorenko, A. N.; Polini, M.; Novoselov, K. S. Graphene Plasmonics. *Nat. Photon.* **2012**, *6*, 749−758.

(2) Clavero, C. Plasmon-Induced Hot-Electron Generation at Nanoparticle/Metal-Oxide Interfaces for Photovoltaic and Photocatalytic Devices. *Nat. Photon.* **2014**, *8*, 95−103.

(3) Xie, L.; Ling, X.; Fang, Y.; Zhang, J.; Liu, Z. Graphene as a Substrate to Suppress Fluorescence in Resonance Raman Spectroscopy. *J. Am. Chem. Soc.* **2009**, *131*, 9890−9891.

(4) Goncalves, G.; Marques, P. A.; Granadeiro, C. M.; Nogueira, H. I.; Singh, M. K.; Grácio, J. Surface Modification of Graphene Nanosheets with Gold Nanoparticles: The Role of Oxygen Moieties at Graphene Surface on Gold Nucleation and Growth. *Chem. Mater.* **2009**, *21*, 4796−4802.

(5) Vianna, P. G.; Grasseschi, D.; Costa, G. K. B.; Carvalho, I. C. S.; Domingues, S. H.; Fontana, J.; de Matos, C. J. S. Graphene Oxide/Gold Nanorod Nanocomposite for Stable Surface-Enhanced Raman Spectroscopy. *ACS Photonics* **2016**, *3*, 1027−1035.

(6) Thareja, V.; Esfandyarpour, M.; Kik, P. G.; Brongersma, M. L. Anisotropic Metasurfaces as Tunable SERS Substrates for 2D Materials. *ACS Photonics* **2019**, *6*, 1996−2004.

(7) Biroju, R. K.; Choudhury, B.; Giri, P. K. Plasmon-Enhanced Strong Visible Light Photocatalysis by Defect Engineered Cvd Graphene and Graphene Oxide Physically Functionalized with Au Nanoparticles. *Catal. Sci. Technol.* **2016**, *6*, 7101−7112.

(8) Biroju, R. K.; Giri, P. K. Defect Enhanced Efficient Physical Functionalization of Graphene with Gold Nanoparticles Probed by Resonance Raman Spectroscopy. *J. Phys. Chem. C* **2014**, *118*, 13833−13843.

(9) Ananthoju, B.; Biroju, R. K.; Theis, W.; Dryfe, R. A. W. Controlled Electrodeposition of Gold on Graphene: Maximization of the Defect-Enhanced Raman Scattering Response. *Small* **2019**, *15*, 1901555.

(10) Biroju, R. K.; Giri, P. K.; Dhara, S.; Imakita, K.; Fujii, M. Graphene-Assisted Controlled Growth of Highly Aligned Zno Nanorods and Nanoribbons: Growth Mechanism and Photoluminescence Properties. *ACS Appl. Mater. Interfaces* **2014**, *6*, 377−387.

(11) Gong, T.; Zhu, Y.; Zhang, J.; Ren, W.; Quan, J.; Wang, N. Study on surface-enhanced Raman scattering substrates structured with hybrid Ag nanoparticles and few-layer graphene. *Carbon* **2015**, *87*, 385−394.

(12) Gong, T.; Zhang, J.; Zhu, Y.; Wang, X.; Zhang, X.; Zhang, J. Optical properties and surface-enhanced Raman scattering of hybrid structures with Ag nanoparticles and graphene. *Carbon* **2016**, *102*, 245−254.

(13) Quan, J.; Zhang, J.; Li, J.; Zhang, X.; Wang, M.; Wang, N.; Zhu, Y. Three-dimensional AgNPs-graphene-AgNPs sandwiched hybrid nanostructures with sub-nanometer gaps for ultrasensitive surface-enhanced Raman spectroscopy. *Carbon* **2019**, *147*, 105−111.

(14) Li, X.; Cai, W.; An, J.; Kim, S.; Nah, J.; Yang, D.; Piner, R.; Velamakanni, A.; Jung, I.; Tutuc, E.; Banerjee, S. K.; Colombo, L.; Ruoff, R. S. Large Area Synthesis of High-Quality Graphene Films on Copper Foils. *Science* **2009**, *324*, 1312−1314.

(15) Lin, Y.-C.; Lu, C.-C.; Yeh, C.-H.; Jin, C.; Suenaga, K.; Chiu, P.-W. Graphene Annealing: How Clean Can It Be? *Nano Lett.* **2011**, *12*, 414−419.

(16) Goel, R.; Awasthi, V.; Rai, P.; et al. Design of Polarization Independent SERS Substrate with Raman Gain Evaluated Using Purcell Factor. *Plasmonics* **2021**, *16*, 1365−1373.

(17) Awasthi, V.; Malik, P.; Goel, R.; Srivastava, P.; Dubey, S. K. "Repeated thermally deposited and annealed gold thin films as SERS-active substrate," in *Conference on Lasers and Electro-Optics, Technical Digest Series*; (Optica Publishing Group, 2022), paper JTh3B.33.

(18) Malik, P.; Awasthi, V.; Goel, R.; Ghosh, S.; Dubey, S. K.; Srivastava, P. "Au coated Femtosecond Laser based patterned non-stoichiometric Silicon Nitride films as SERS substrate," in *Optical Sensors and Sensing Congress 2022 (AIS, LACSEA, Sensors, ES)*; Technical Digest Series (Optica Publishing Group, 2022), paper LM2B.4.

(19) Awasthi, V.; Goel, R.; Rai, P.; Dubey, S. K. Detection of nitrogenous and nitro-aromatic compound with thin gold films roughened by cold argon plasma as SERS-active substrate. *Surf. Interfaces* **2022**, *28*, 101556.

(20) Palik, E. D. *Handbook of Optical Constants of Solids*; Academic Press, 1985, DOI: 10.1016/C2009-0-20920-2

(21) Johnson, P. B.; Christie, R. W. Optical constants of the noble metals. *Phys. Rev. B* **1972**, *6*, 4370−4379.

(22) Falkovsky, L. A.; Pershoguba, S. S. Optical far-infrared properties of a graphene monolayer and multilayer. *Phys. Rev. B* **2007**, *76*, 1534.

(23) Ferrari, A. C.; Basko, D. M. Raman Spectroscopy as a Versatile Tool for Studying the Properties of Graphene. *Nat. Nanotechnol.* **2013**, *8*, 235−246.

(24) Ferrari, A. C.; et al. Raman Spectrum of Graphene and Graphene Layers. *Phys. Rev. Lett.* **2006**, *97*, 187401.

(25) Cançado, L. G.; Jorio, A.; Ferreira, E. H. M.; Stavale, F.; Achete, C. A.; Capaz, R. B.; Moutinho, M. V. O.; Lombardo, A.; Kulmala, T. S.; Ferrari, A. C. Quantifying Defects in Graphene Via Raman Spectroscopy at Different Excitation Energies. *Nano Lett.* **2011**, *11*, 3190−3196.

(26) Lee, J.; Novoselov, K. S.; Shin, H. S. Interaction between Metal and Graphene: Dependence on the Layer Number of Graphene. *ACS Nano* **2010**, *5*, 608−612.

(27) Biroju, R. K.; Rajender, G.; Giri, P. K. On the Origin and Tunability of Blue and Green Photoluminescence from Chemically

Derived Graphene: Hydrogenation and Oxygenation Studies. *Carbon* **2015**, *95*, 228−238.
(28) Wang, H.; et al. Doping Monolayer Graphene with Single Atom Substitutions. *Nano Lett.* **2012**, *12*, 141−144.
(29) Cong, C.; Yu, T.; Saito, R.; Dresselhaus, G. F.; Dresselhaus, M. S. Second-Order Overtone and Combination Raman Modes of Graphene Layers in the Range of 1690-2150 Cm-1. *ACS Nano* **2011**, *5*, 1600−1605.
(30) Rao, R.; Podila, R.; Tsuchikawa, R.; Katoch, J.; Tishler, D.; Rao, A. M.; Ishigami, M. Effects of Layer Stacking on the Combination Raman Modes in Graphene. *ACS Nano* **2011**, *5*, 1594−1599.
(31) Gan, Y.; Sun, L.; Banhart, F. One- and Two-Dimensional Diffusion of Metal Atoms in Graphene. *Small* **2008**, *4*, 587−591.
(32) Ng, H. T.; Li, J.; Smith, M. K.; Nguyen, P.; Cassell, A.; Han, J.; Meyyappan, M. Growth of Epitaxial Nanowires at the Junctions of Nanowalls. *Science* **2003**, *300*, 1249.
(33) Bratescu, M. A.; Saito, N. Charge Doping of Large-Area Graphene by Gold-Alloy Nanoparticles. *J. Phys. Chem. C* **2013**, *117*, 26804−26810.
(34) Ling, X.; Xie, L.; Fang, Y.; Xu, H.; Zhang, H.; Kong, J.; Dresselhaus, M. S.; Zhang, J.; Liu, Z. Can Graphene Be Used as a Substrate for Raman Enhancement? *Nano Lett.* **2010**, *10*, 553−561.
(35) Du, Y.; Zhao, Y.; Qu, Y.; Chen, C.-H.; Chen, C.-M.; Chuang, C.-H.; Zhu, Y. Enhanced Light-Matter Interaction of Graphene-Gold Nanoparticle Hybrid Films for High-Performance Sers Detection. *J. Mater. Chem. C* **2014**, *2*, 4683−4691.
(36) Singh, N. S.; Mayanglambam, F.; Nemade, H. B.; Giri, P. K. Plasma-Treated Graphene Surfaces for Trace Dye Detection Using Surface-Enhanced Raman Spectroscopy. *ACS Appl. Nano Mater.* **2022**, *5*, 6352−6364.
(37) Schedin, F.; Lidorikis, E.; Lombardo, A.; Kravets, V. G.; Geim, A. K.; Grigorenko, A. N.; Novoselov, K. S.; Ferrari, A. C. Surface-Enhanced Raman Spectroscopy of Graphene. *ACS Nano* **2010**, *4*, 5626.
(38) Xu, C.; Wang, X. Fabrication of Flexible Metal-Nanoparticle Films Using Graphene Oxide Sheets as Substrates. *Small* **2009**, *5*, 2212−2217.
(39) Muszynski, R.; Seger, B.; Kamat, P. V. Decorating Graphene Sheets with Gold Nanoparticles. *J. Phys. Chem. C* **2008**, *112*, 5263−5266.

https://doi.org/10.1021/acsomega.2c07706
ACS Omega 2023, 8, 4344−4356